

Toward automated detection of light echoes in synoptic surveys: considerations on the application of the Deep Convolutional Neural Networks

XIAOLONG LI,¹ FEDERICA B. BIANCO,^{1,2,3} GREGORY DOBLER,^{2,1,3} ROEE PARTOUSH,⁴ ARMIN REST,^{5,4}
 TATIANA ACERO-CUELLAR,^{1,6} RILEY CLARKE,¹ WILLOW FOX FORTINO,¹ SOMAYEH KHAKPASH,¹ AND MING LIAN¹

¹Department of Physics and Astronomy, University of Delaware, Newark, DE 19716-2570, USA

²Biden School of Public Policy and Administration, University of Delaware, Newark, DE 19716-2570, USA

³Data Science Institute, University of Delaware, Newark, DE 19716-2570, USA

⁴Department of Physics and Astronomy, Johns Hopkins University, 3400 North Charles Street, Baltimore, MD 21218, USA.

⁵Space Telescope Science Institute, 3700 San Martin Dr., Baltimore, MD 21218, USA

⁶Observatorio Astronómico Nacional, Universidad Nacional de Colombia, Bogotá, Colombia

ABSTRACT

Light Echoes (LEs) are the reflections of astrophysical transients off of interstellar dust. They are fascinating astronomical phenomena that enable studies of the scattering dust as well as of the original transients. LEs, however, are rare and extremely difficult to detect as they appear as faint, diffuse, time-evolving features. The detection of LEs still largely relies on human inspection of images, a method unfeasible in the era of large synoptic surveys. The Vera C. Rubin Observatory Legacy Survey of Space and Time, LSST, will generate an unprecedented amount of astronomical imaging data at high spatial resolution, exquisite image quality, and over tens of thousands of square degrees of sky: an ideal survey for LEs. However, the Rubin data processing pipelines are optimized for the detection of point-sources and will entirely miss LEs. Over the past several years, Artificial Intelligence (AI) object detection frameworks have achieved and surpassed real-time, human-level performance. In this work, we prepare a dataset from the ATLAS telescope and test a popular AI object detection framework, You Only Look Once, or YOLO, developed in the computer vision community, to demonstrate the potential of AI in the detection of LEs in astronomical images. We find that an AI framework can reach human-level performance even with a size- and quality-limited dataset. We explore and highlight challenges, including class imbalance and label incompleteness, and roadmap the work required to build an end-to-end pipeline for the automated detection and study of LEs in high-throughput astronomical surveys.

1. INTRODUCTION

Light Echoes (LEs) are the reflections of light emitted by transients off of interstellar dust. While photons from a transient can reach us traveling along the line of sight, photons originally directed away from us can be reflected back to earth by favorably oriented dust sheets. The reflected image of the transient will inherit the complexity of the underlying dust structure, with morphological features at arcsecond or even arcminute spatial scales.

LEs provide invaluable information about the dust and the transient sources that originate them. They enable the study of dust and can reveal the dust struc-

ture around a transient in detail (Patat 2005). Through LEs, we have the unique opportunity to re-see ancient transients detected in direct light decades or even centuries ago, and study them with new technology and instrumentation (Rest et al. 2011) so that LEs can be used, for example, to classify historical supernovae (Rest et al. 2005, 2008a,b). This was in fact how the Tycho and Cas A supernovae were classified (Rest et al. 2008b; Krause et al. 2008a,b). Finally, LEs can also provide a 3D view of an astronomical phenomenon, enabling the study of asymmetry of individual supernovae and supernova classes (Rest et al. 2011; Finn et al. 2016).

LEs are rare phenomena, as they require the serendipity of a bright transient and of the presence of a dust sheet oriented correctly to reflect the light towards the Earth. They are also extremely difficult to detect. The magnitude of a LE is ~ 10 times fainter than its tran-

sient source (Patat 2005). Thus, LEs bright enough for detection are extremely rare. Furthermore, the dynamic and complex dust environment makes their shape irregular and their identification more difficult than the identification of point-source transients. To date, no algorithm has proven successful in simultaneously detecting and localizing LEs in untargeted image surveys, and visual inspection of template subtracted images is the framework generally adopted for detection (see section 3).

The next generation of ground-based synoptic surveys, and in particular the Rubin Observatory Legacy Survey of Space and Time (LSST), will make visual-inspection of images unsuitable for practical purposes. Rubin LSST is scheduled to observe the sky continuously for 10 years starting in 2024. The telescope will have an 8.4 m (6.5 m effective) primary mirror, a 9.6 deg² field of view, and a 3.2 Gigapixel camera which will produce 20Tb of information-dense data each night (Ivezić et al. 2019). LSST’s unique survey capability in the time domain and exquisite image quality will enable a vast and diverse range of scientific investigations. The LSST, with its unique combination of sensitivity, wide field of view, and dense observing cadence, has the capacity to revolutionize LE studies, pushing the field from novelty detections into statistically relevant regimes. But with nearly 1000 images each night for 10 years, it will become impossible to visually inspect the images to detect the LEs. An automated detection pipeline for LEs is needed to analyze the enormous outputs of this telescope.

The LSST data processing pipeline under development is scoped to detect millions of alerts every night: anything that significantly changes (at a 5- σ level) in the night sky from a reference image. However, the pipeline is designed for point-like sources, and it will entirely miss diffuse and extended transients, such as LEs. Our ultimate goal is to create an end-to-end pipeline for the detection and study of LEs in the LSST era. With this paper, we set the stage by exploring the potential of region-based Convolutional Neural Networks (CNNs) for LE discovery.

Automating the detection of LEs is a complex computer vision problem. Over the past several years, deep learning has proven successful in discovering intricate structures in high-dimensional data, and especially in images (LeCun et al. 2015). Deep learning-based object detection frameworks have achieved real-time, high-accuracy performance (Zhao et al. 2019) that matches or surpasses that of humans. Deep Neural Networks (DNNs) have recently been used in the detection and study of astronomical sources, including the detection of galaxy clusters (Chan & Stott 2019), gravitational

lenses (Davies et al. 2019), supernova remnants (Liu et al. 2019), and more. DNNs have also been applied to the detection of LEs in Bhullar et al. (2021). This work produced a slide window detection model, ALED, which is based on a capsule CNN architecture (Sabour et al. 2017). We compare this model in detail with our region-based model in the Results section of this paper (see section 5).

In this paper, we present a proof-of-concept LE detection pipeline based on a robust and proven AI object detection framework, YOLOv3 (Redmon & Farhadi 2018), applied to the Asteroid Terrestrial-impact Last Alert System (ATLAS, Tonry et al. 2018) telescope data. ATLAS provides a wide-field multi-epoch survey. Compared to the LSST, the survey for which we ultimately want to build a pipeline, the ATLAS survey is shallow (mag range 11–19.5) and coarse (resolution 1.86''/pixel); however, these data provide an excellent test-bed that allows us to demonstrate the potential of AI to detect LEs, and to explore the subtleties and nuances of architectures suitable to accomplish this task.

This paper is organized as follows. We introduce the LE phenomenon and its history of discovery in section 2. In section 3 we describe how our dataset is prepared. In section 4, we present our detection framework, the definition of detection and the method of evaluation. The results of our model are discussed in section 5. Finally, in section 6 we highlight challenges and the future work required to build an end-to-end automated pipeline for the detection and study of LEs.

2. HISTORICAL NOTE ON LIGHT ECHOES

LEs were first discovered around Nova Persei 1901 (Ritchey 1901, 1902). Since then, LEs have been observed from a variety of sources, including variable stars: Galactic Nova Sagittarii (Swope 1940), Galactic Cepheid RS Puppis (Havlen 1972), Nova Cygni (Bode & Evans 1985), OH 231.8+4.2 (Kastner et al. 1992, 1998), V838 Monocerotis (Bond et al. 2003), the T Tauri star S CrA (Ortiz et al. 2010), the Herbig Ae/Be star R CrA (Ortiz et al. 2010); historical supernovae, of which we have centuries old records or that we only know from their remnants: SNR 0519-69.0 (Rest et al. 2005), SNR 0509-67.5 (Rest et al. 2005), SNR N103B (Rest et al. 2005), Cas A (Rest et al. 2007, 2008a; Krause et al. 2008a), Tycho (Rest et al. 2007, 2008a; Krause et al. 2008b); modern supernovae, observed directly with modern astrophysical instrumentation as well, as in LEs: 1987A (Crotts 1988; Sunzeff et al. 1988), 1980K (Sugerman et al. 2012), 1991T (Schmidt et al. 1994; Sparks et al. 1999), 1993J (Sugerman & Crotts 2002; Liu et al. 2003), 1995E (Quinn et al. 2006), 1998bu(Cappellaro

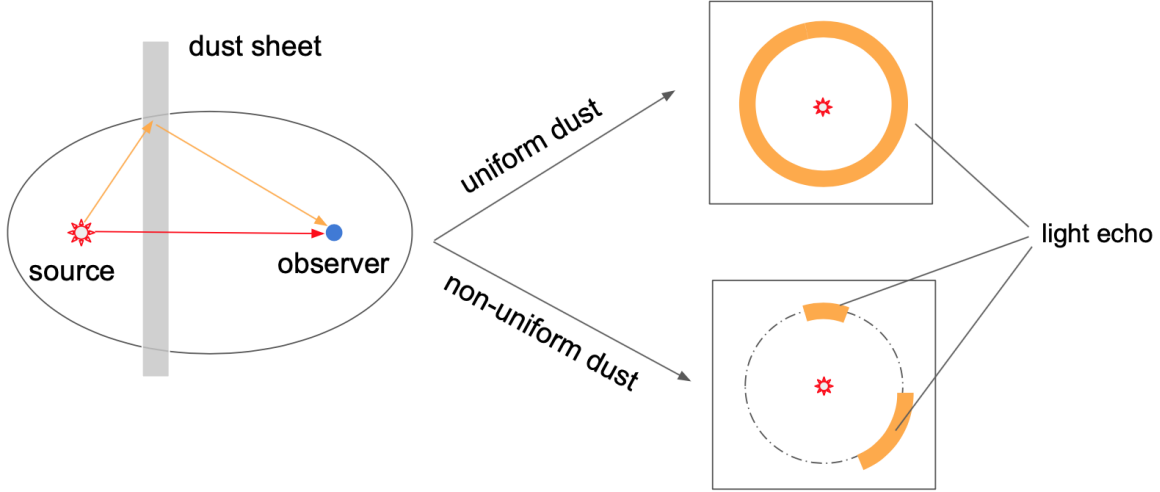


Figure 1. A slice of the geometry of the LE phenomenon (left) and its projection on the plane of the sky (right) in the case of a continuous dust sheet (top) and dust filaments (bottom). At each point in time, for every transient there is an ellipsoidal surface with foci at the earth and the transient. All points on the ellipsoid reflect light from the transient that arrive on earth at the same time and the ellipsoid itself expands over time. Due to the increase in path length, LEs reach the observer after the light from the original transient. On the plane of the sky, we see the cross-section of the reflection ellipsoid, yet not all LEs are circles: in most cases only a portion of the ellipsoid will have dust that reflects the light echo towards Earth. Most observed LEs are only arcs of a circle.

et al. 2001), 1999ev (Maund & Smartt 2005), 2002hh (Welch et al. 2007; Otsuka et al. 2011), 2003gd (Sugerman 2005; Van Dyk et al. 2006; Otsuka et al. 2011), 2004et (Otsuka et al. 2011), 2006X (Wang et al. 2008; Crotts & Yourdon 2008), 2006bc (Otsuka et al. 2011; Gallagher et al. 2012) 2006gy (Miller et al. 2010), 2007it (Andrews et al. 2011), 2007af (Drozdov et al. 2015), 2008bk (Van Dyk 2013), 2012aw (Van Dyk et al. 2015), 2014J (Crotts 2015; Yang et al. 2017), 2016adj (Sugerman & Lawrence 2016); and the massive eruptive stellar system η Carinae (Rest et al. 2012; Prieto et al. 2014; Smith et al. 2018a,b).

The first systematic study of the phenomenon appeared in 1939 (Couderc 1939), and the theoretical framework was formalized further in Sugerman (2003); Tylenda (2004); Patat (2005); Patat et al. (2006); Rest et al. (2011). As shown in Figure 1, at each point in time, for any given transient there is an ellipsoidal surface with foci at the Earth and the transient. If there is dust with the proper orientation on the ellipsoidal surface, photons that reach it are reflected towards the Earth. All points on the ellipsoid reflect light from the transient that arrives at the Earth at the same time (Patat 2005; Patat et al. 2006; Rest et al. 2011). Because of the increased path length, reflected light arrives at a delay compared to light traveling the direct path from the transient to the Earth. As time goes by, the ellipsoid expands and so does the travel path of LE

light, giving us the opportunity to re-observe transients, even historical transients, that were directly observed centuries ago (Rest et al. 2005, 2007, 2008a; Rest et al. 2011; Rest et al. 2012).

In astronomical images, LEs appear as faint, morphologically diverse, diffused features. When they are reflected by dust directly surrounding the transient, circumstellar dust ejected from stellar eruptions for example, the LEs may appear as rings (see top plot of the right panel in Figure 1). Most commonly, however, and when the source is a centuries-old transient, they take the shape of the dust filaments they reflect along a segment of the reflection ellipsoid (see bottom plot of the right panel in Figure 1).

3. DATA

In this work, we trained an AI model to detect LEs based on a dataset of visually inspected *template subtracted images* from the ATLAS survey.

Template subtracted images can reveal transients that, due to their faint nature or the complex environment in which they arise (such as supernovae near the center of a Galaxy or a star forming region), are invisible to the naked eye in the original images. Template subtraction, or Difference Image Analysis (DIA), was developed as a technique for detecting transients and

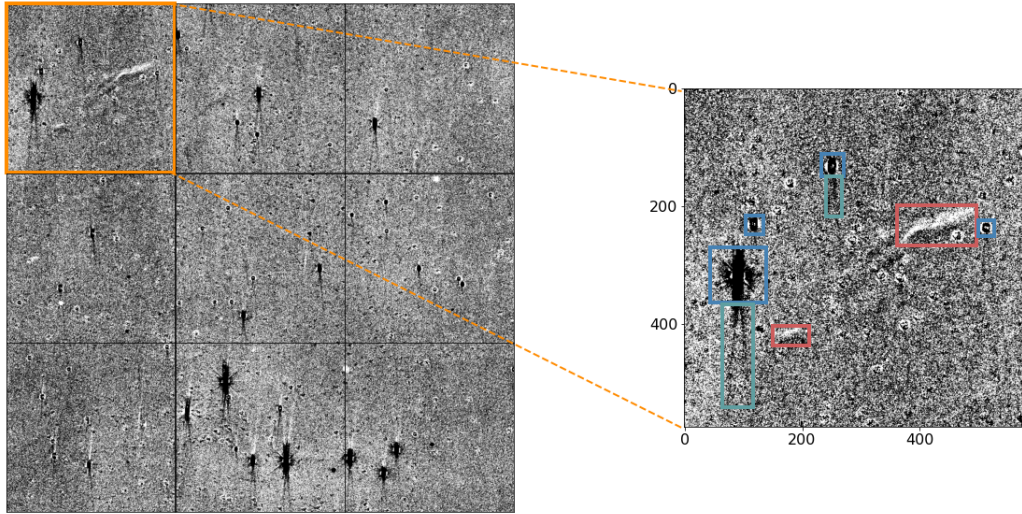


Figure 2. An example of a template-subtracted (“difference”) image from the ATLAS survey (see section 3 for details). The native resolution of the difference image is 1800×1800 pixels, corresponding to about 1 square degree. The images are template-subtracted to aid detectability of the faint, time-evolving LE features. The full-frame image (left) contains a LE in the top left corner, as well as stars and artifacts throughout. Because of the rarity of LEs, in order to mitigate class imbalance between stars and LEs in our dataset, we split each ATLAS image into 9 tiles and select only the tiles that contain LEs. The top-left tile of this image that contains a LE is marked by an orange frame and is reproduced to the right with boxes corresponding to saturated stars, star streaks, and LEs are shown in blue, teal, and red respectively.

Table 1. Technical specifications of the ATLAS system camera

Parameters	Value
Camera	Acam
Format (pixels)	10560×10560
Pixel Scale (arcsec)	1.86
FOV(degree)	5.375×5.375
Number of filters	7

NOTE—Additional specifications are available in <https://atlas.fallingstar.com/specifications.php>

Table 2. LE data from ATLAS

Parameters	Value
RA	0 360
DEC	-40 90
Epochs (MJD)	58400, 58450, 58500, 58600, 58650
Total number of images	46800×5
Filter	<i>r</i>
Image size after DIA processing	1800×1800 pixels (1 \times 1 degree)
Images with LEs	17 \times 5

monitoring microlensing events (Norgaard-Nielsen et al. 1989; Crotts 1992; Phillips & Davis 1995). Models based on the Optimal Image Subtraction (OIS) method (Alard & Lupton 1998) are widely deployed to survey-based searches for moving objects and changing astronomical phenomena. Two images, of which one is considered a “template”, are aligned, PSF-matched, and subtracted from one-another. The template itself can be a single, or more commonly a composite, image (generally from the same survey) with image properties that reach or ap-

proach the highest image quality the survey is capable of acquiring in terms of overall noise, spatial resolution, and depth. After subtraction, the static background vanishes while any time-dependent phenomena, such as transients or moving objects, appear as a deviation from the 0-flux average.

In practice, the DIA process is prone to the generation of artifacts that complicate the detection of transients in general, and LEs in particular.

We assembled a dataset from template subtracted images from the ATLAS survey (Tonry et al. 2018). The telescope has a 5.375×5.375 degree field of view, and

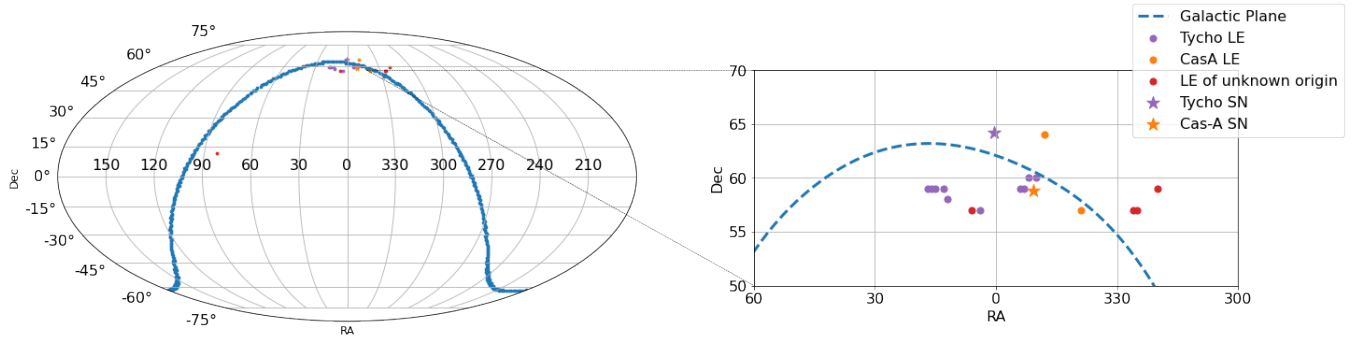


Figure 3. The sky positions of 17 LEs contained in our final dataset. Ten of them are from the Tycho SN, and two are from Cas A. The rest have positions and orientations that are inconsistent with both Tycho and Cas A and are of as-of-yet unknown origin. LEs are preferentially found in high-dust content regions, such as near the Galactic plane, which is indicated by a thick blue line in this plot. The right panel shows a zoom-in view of the region containing the majority of the LEs recovered in our data. Table 3 contains the coordinate of each of the LEs in this figure.

the observational system is designed for the detection of asteroids. Table 1 shows the ATLAS system and survey characteristics, including the pixel resolution, sensitivity, filters used, and image size in pixels. Table 2 shows the characteristics of the ATLAS data used in this paper.

Each image produced by the ATLAS DIA pipeline is originally 1800×1800 pixels, covering a $\sim 1 \times 1$ degree field of the sky. In the ATLAS difference images (*e.g.* Figure 2) we see several artifacts and imperfections produced by the DIA that complicate the detection of LEs: we notice residuals corresponding to saturated stars, with streaks typically associated with each saturated star. We also see residuals corresponding to stars below the saturation limit, due to sub-optimal image alignment or PSF matching.

We visually inspected images within a sky region ranging from DEC 40° – 90° , RA 0° – 360° . This corresponds to about 234,000 inspected images as each field is observed at five different epochs (see Table 2). We select 17 images that host LEs with sufficient signal-to-noise ratio (*SNR*) to enable unambiguous detection by human visual inspection.¹ These LEs primarily originate from the Cas A and Tycho SNe, but we also found and included several LE-groups in our training set that are inconsis-

tent with originating from either of those SNe and whose source is being investigated by our team. Note that hereafter we define a LE as a single contiguous dust filament lit by a transient’s light, and a LE-group as an ensemble of individual LEs originating from a complex structure of dust with many filaments lit at the same time. Most LEs in our images are in LE-groups. Figure 2 shows an example image from ATLAS with a LE-group composed of two LEs in the top-left corner.

Figure 3 shows the sky-locations of the 17 LEs; their coordinates and transient sources are listed in Table 3. These constitute our dataset, the size of which is significantly smaller than those traditionally used to train region-based CNN object detection models in the computer vision literature (*e.g.*, the original implementation of YOLO was trained on ImageNet, Russakovsky et al. 2015, which consisted of more than 1,000,000 images with 1,000 different object classes).

In each image, we draw bounding boxes for three classes, LEs, stars and “other”, which is a catch-all class for additional features and artifacts that may be present in an image, such as star streaks, satellites, *etc.* Notice that there is a certain amount of arbitrariness in the choice of the location and extent of a LE bounding box. Our bounding boxes strive to delimit each LE but end up, in many cases, including multiple LEs from the same LE-group. We will return to this point when we describe our strategy for model evaluation in subsection 4.2. We build our dataset in the COCO (Lin et al. 2014) format using labelme².

Because LEs are rare phenomena, much rarer than stars, there exists a large class imbalance between the number of objects in our three classes, and we note that

¹ We note here that defining the *SNR* of a LE is a complex task: the morphology is complex and the edges of the feature are not trivial to identify. We find that a functional definition of *SNR* can exploit the characteristic “dipole” morphology. As the light travels across a sheet of dust, it illuminates different regions. In a difference image this results in clusters of pixel values positive on one side and negative on the other (pointing in the direction of the original transient). Our functional definition of LE *SNR* then exploits the contrast in the dipole and the size of the region covered by the LE, measured through a simple segmentation procedure, as $SNR_{LE} = IQR/\log_{10}(N_{pix})$. Ultimately, we find that this metric generally tracks the score our model assigns to our LEs.

² <https://github.com/wkentaro/labelme>

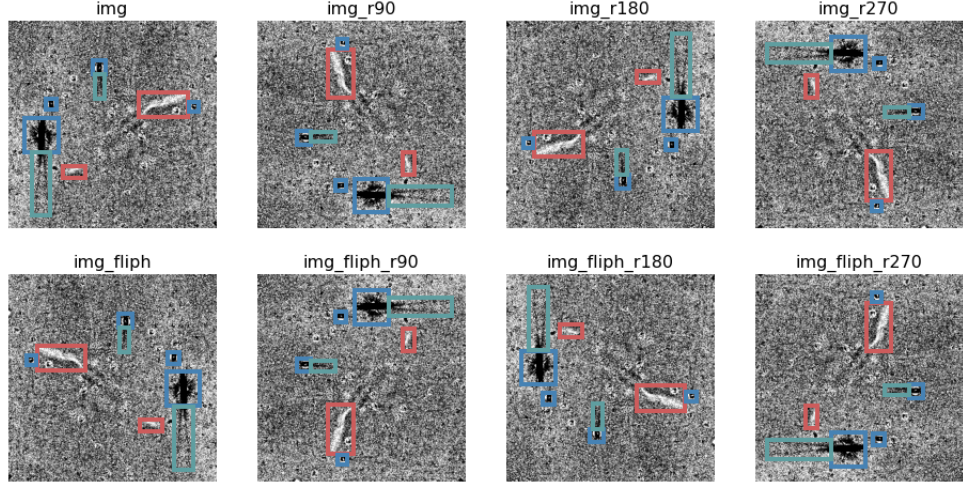


Figure 4. Image augmentations applied to the ATLAS dataset: the images generated by subdividing the original ATLAS data are first flipped horizontally, and then rotated by 90, 180, and 270 degrees. This augmentation increases our dataset size by a factor of 8.

Table 3. Observed ATLAS LEs detected by visual inspection

RA	DEC	Gal l	Gal b	Source
4.0	57.0	118.1	-5.5	Tycho
6.0	57.0	119.2	-5.7	unknown
12.0	58.0	122.5	-4.9	Tycho
13.0	59.0	123.0	-3.9	Tycho
15.0	59.0	124.0	-3.9	Tycho
16.0	59.0	124.6	-3.8	Tycho
17.0	59.0	125.1	-3.8	Tycho
82.0	12.0	192.3	-12.4	unknown
320.0	59.0	98.5	6.6	unknown
325.0	57.0	99.1	3.3	unknown
326.0	57.0	99.5	2.9	unknown
339.0	57.0	105.3	-1.2	Cas A
348.0	64.0	112.3	3.2	Cas A
350.0	60.0	111.7	-0.9	Tycho
352.0	60.0	112.7	-1.2	Tycho
353.0	59.0	112.8	-2.3	Tycho
354.0	59.0	113.3	-2.5	Tycho

NOTE—The coordinates reported are for the difference image centroid.

imbalance in the training dataset can potentially introduce a bias in learning (Oksuz et al. 2020) and should therefore be addressed. The root of this potential bias lies in the fact that over-represented classes have more influence on the loss function, when the loss function is calculated as an average or median across all examples. Class imbalance in the training of machine learning models might thus lead to better performance on over-represented classes relative to under-represented ones.

However, we also note that in-class diversity and the SNR of individual objects are other important factors which may either reduce or enhance this effect. While we will implement a modification of the YOLO loss function that will help mitigate the risk of this bias (see section 4), we also address the class imbalance in data preparation. We split the images into 576×576 pixel sub-images and only include in our dataset the image segments that host LEs.³

We apply three data augmentation techniques to expand our dataset: we first flip each image horizontally, then rotate each image by 90°, 180°, and 270°. Figure 4 shows an example of the results of image augmentation and Table 4 shows the number of images available in our dataset after each step of our augmentation process. The final dataset contains 224 images, 576 boxes labeled as LEs, and 1248 labeled as stars.

On average, each image contains three LEs, six stars, and four “other” objects. Figure 5 shows the distribution of number of bounding boxes for both LEs and stars in each image, and the size distribution of the boxes. The size of the bounding box is measured as the ratio of the diagonal of the box and the diagonal of the image. The mean size of LE boxes (as well as “other” boxes) in these units is ~ 0.1 (~ 3 arcmin), while the stars are smaller, ~ 0.06 (~ 1.8 arcmin).

Finally, the pixel values in images that are fed into a neural network need to be appropriately scaled. Unlike normal 8-bit color RGB images, imaging data from the ATLAS telescope is stored as FITS files (Wells &

³ YOLOv3 can accept input images at any size, however we choose 576 for potential future work since some CNNs model requires the input size to be divisible by 64.

Table 4. Augmentation details

Parameters	Value	Train/Test
Initial number of images	28	20/8
After flipping	56	40/16
After rotating	224	160/64

(Greisen 1979). In our data, which is entirely comprised of template subtracted images, the FITS pixel values range from about -10000 to 5000. To feed the images as input to a traditional neural network architecture, however, a normalization is required. In order to constrain the pixel value range while minimizing the loss of information, we clip the raw FITS array to $[-10, 10]$, a range that contains about 95% of the pixel values in our data. We then standardize the clipped images by subtracting the mean and dividing the result by the standard deviation of the distribution of pixel values in the clipped FITS images.

Compared with other benchmark computer vision datasets, such as MS COCO (Lin et al. 2014) or Pascal VOC (Everingham et al. 2010), the dataset we have is far from ideal. First, as discussed earlier, the total number of images is small, even after augmentation. Second, the labels are incomplete. We labeled only two classes, while there are many kinds of objects contained in these images, such as satellites, artifacts, or star streaks, which may confuse the model. We classify all these objects under the same “other” label. Third, the LE set is extremely small and all LEs are from a limited set of sources, primarily Tycho and Cas A, and may not span the full range of morphologies of the phenomenon. However, this dataset is a starter dataset for building a LE detection model, and used as a proof-of-concept here to explore the potential of AI applications to LE detection and the architectural modifications required to adapt existing region-based CNNs to this problem.

4. METHODOLOGY

Beginning in the late 1990s, the field of automated image recognition has been dominated by a family of AI models called Convolutional Neural Networks (CNNs, LeCun et al. 1989). Today, CNNs – alongside “attention”-based “transformer” models (e.g., Vaswani et al. 2017) – remain one of the primary families of models for image recognition tasks. Object detection frameworks based on CNNs have achieved and surpassed human performance. There are two main CNN frameworks for task of detecting (Zhao et al. 2019) and localizing objects in images (i.e., region-based CNNs): re-

gion proposal-based two-stage methods that first propose regions with one CNN and an object in those regions with another (Girshick et al. 2014; Girshick 2015; Ren et al. 2015) and single-stage methods (e.g., Redmon et al. 2016) that identify and classify regions through a single deep CNN model. In this paper we focus on single-stage CNN methods, using the third publicly available version of the “*You Only Look Once*” (YOLOv3) model (Redmon & Farhadi 2018).

A few choices have to be made and challenges have to be faced for the detection of LEs which are unlike those traditionally encountered when detecting common computer vision targets in the field of object identification. These challenges are shared by other fields of research (e.g. other applications of AI to astrophysical tasks, or in the medical field) but in combination they may be unique or at least rare.

- LEs are not finite objects: they exist at all levels of SNR and their edges blend into the background as the dust that reflects them blends into empty space and the light they reflect fades. Thus we cannot aspire to be complete in our human labeling because where LEs blend into the noise human detection fails. Since our training set is not complete, we have to teach the CNN both what is and what is not a LE: a multi-label model. In this initial work we only train the model to identify LEs, stars, and a limited number of artifacts.
- Of the many features in an image, LEs are an extremely rare occurrence. Stars and galaxies, transients and variable phenomena, moving objects, and several artifacts overwhelm the image searches. Detection of rare features is a problem often encountered in medical applications of computer vision (Sánchez Fernández et al. 2020, and references therein). We explore the detection of LEs in a subset of our data where each image contains at least one LE (as described in section 3) because we want to focus on the architectural choices that enable the detection of LE features.
- Putting bounding boxes around LEs requires us to make choices that are, to some extent, arbitrary: each LE inherits a complex structure from the underlying dust and most LE filaments are connected into complex structures (LE-group, section 3). While we strive for consistency in setting the bounding boxes around isolated filaments, we cannot expect that the model will generate bounding boxes that exactly overlap each one of the training bounding boxes. We address this issue

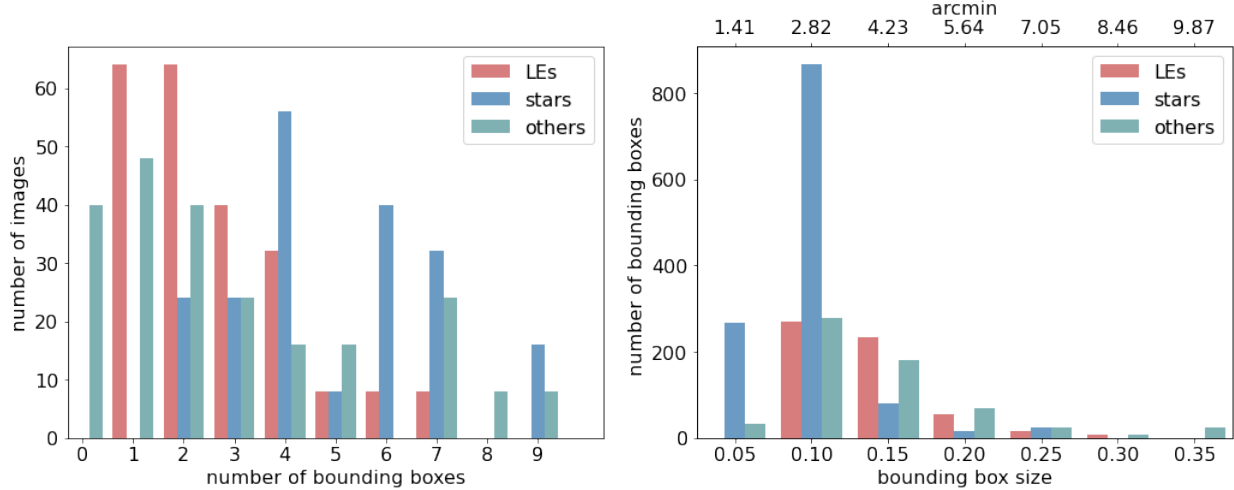


Figure 5. The distribution of number of bounding boxes per image (left) and bounding box sizes across all images (right) for the two labeled classes: LEs, stars, and “other” (including satellite and star streaks and other artifacts). After augmentation (see Figure 4), the final dataset contains 224 images, 584 boxes labeled as LEs, 1256 labeled as stars, and 648 as other. On average, each image contains 3 LEs, 6 stars, and 3 “other” objects. The size of the bounding boxes is measured as the ratio of the diagonal of the box to the diagonal of the image. In these units, the mean size of LE and “other” boxes is ~ 0.1 (~ 3 arcmin), while the stars are smaller, ~ 0.06 (~ 1.8 arcmin).

by modifying the region-based CNN loss (see subsection 4.1) exploring various approaches to mitigating this problem, including the application of focal loss (Lin et al. 2017; Vaswani et al. 2017), and with a specific definition of True and False positives (see subsection 4.2) that differ in the training and evaluation phases.

4.1. YOLOv3

YOLO (You Only Look Once Redmon & Farhadi 2018) is a popular single-stage regression/classification region-based framework where “regression” refers to the identification of regions of interest through regression of bounding box coordinates and “classification” refers to the classification of the object inside of those bounding box regions. Feature extraction and object localization are integrated into a single deep neural network model. An input image is split into an $S \times S$ grid of cells. Each cell is responsible for both class prediction and bounding boxes regression of objects whose centers fall inside the cell. In other words, through a DNN model, an input image is mapped to a tensor with the shape $S \times S \times N_b \times (5 + N_c)$, where N_b is the number of predefined anchor boxes assigned to each cell, each containing the probabilities p_c for each of the N_c classes. The number 5 comes from having one parameter C for the confidence that an object is present in the bounding box and four parameters to define the position and size of the bounding box b_x, b_y, b_h, b_w .

In this paper we adopt the architecture of YOLOv3 (Redmon & Farhadi 2018). We note that our choice of

YOLOv3 is motivated by a desire to use a model that is both “foundational”, in terms of region-based CNN object detection methodology (Girshick et al. 2014; Girshick 2015; Ren et al. 2015; Redmon et al. 2016, see also Sultana et al. 2020 for a review), stable, and with comparable performance to models under active development. That is, one of the goals of this paper is to demonstrate that region-based CNN models can be used for the purpose of detecting LEs in upcoming surveys, and so future work can be aimed at assessing the relative advantages of one particular implementation over another. The YOLOv3 architecture is shown in Figure 6. YOLOv3 uses Darknet-53, which consists of 53 deep convolutional layers, as the backbone network and makes predictions at three scales (1/8, 1/16, and 1/32 the size of the input image).⁴ We pass our 576×576 ATLAS images (each of which contains at least one light echo as described above) through Darknet-53 which, because its architecture includes multiple convolutional layers with strides equal to 2, results in a downsampling to three scales appropriate for the detection of LEs in our sample, 72×72 , 36×36 , and 18×18 pixels. These feature maps are passed to the classifier and bounding box regression

⁴ As pointed out in Redmon & Farhadi (2018), Darknet-53 is a powerful model which has comparable accuracy to ResNet-101 (He et al. 2016) used in Faster RCNN (Ren et al. 2015), but the speed is $1.5\times$ faster. Our preliminary work comparing results based on YOLO with results obtained from Faster RCNN does not suggest that the one-stage YOLO architecture is less suitable for the detection of LEs than a more traditional two-stage RCNN model when comparing model accuracies for the two.

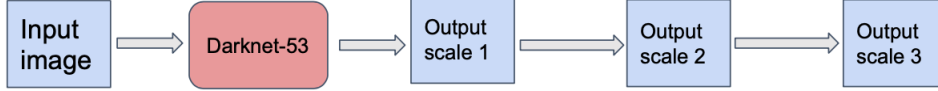


Figure 6. Architecture of the YOLOv3. An input image is mapped to a tensor of shape $S \times S \times N_b \times (5 + N_c)$ through a deep neural network model as described in subsection 4.1. Each cell of the $S \times S$ grid is responsible for both class prediction and bounding boxes regression of objects whose centers fall inside the cell. The YOLOv3 model makes predictions at three size scales (1/8, 1/16, 1/32 of the image size).

network which, for each of these scales, assigns three anchor boxes (regions) of different axis ratio to each grid cell, resulting in $(72 \times 72 + 36 \times 36 + 18 \times 18) \times 3 = 20412$ bounding boxes. The regression network assigns a score for each class to each set of the bounding boxes' coordinates, generating predictions for those 20412 boxes.

The predicted bounding boxes are first filtered by thresholding on the probabilistic classification score p_s , which is the confidence C times the probability p_c that the object is of a certain class, $p_s = Cp_c$, in order to eliminate boxes with a low score. Non-maximum suppression (NMS Neubeck & Van Gool 2006) is then applied to keep only one box when several boxes overlap with each other.

YOLOv3 minimizes a loss function which consists of three parts: confidence loss L_{conf} , classification loss L_{cls} , and bounding box regression loss L_{box} ,

$$L_{total} = L_{conf} + L_{cls} + L_{box}. \quad (1)$$

The confidence loss L_{conf} represents the loss from the confidence probability C (1 if there is an object in the bounding box and 0 for background), while L_{cls} measures the ability make a correct classification. We use a simple cross entropy loss,

$$L_{cls} = \sum_{i=0}^{S^2} \sum_{j=0}^B I_{ij}^{obj} f_{CE}(p_{ij}, \hat{p}_{ij}) \quad (2)$$

where S^2 denotes the three scales of the anchor boxes, and B is the total number of anchor boxes assigned to each grid cell. I_{ij}^{obj} denotes whether there is a object in the cell (it is 1 when there is an object and 0 otherwise), while f_{CE} stands for the cross entropy function given by:

$$f_{CE}(x, y) = -y \log(x) - (1 - y) \log(1 - x). \quad (3)$$

The number of background anchor boxes is typically much larger than the number of foreground anchor boxes. To address this problem, Lin et al. (2017) proposed to use the “focal” loss, which adds a factor to the cross entropy loss. We adopt a similar approach for the detection of LEs, since as shown in section 3, on average there are only 3 LEs in each image. We redesign

$$L_{conf},$$

$$\begin{aligned} L_{conf} = & \sum_{i=0}^{S^2} \sum_{j=0}^B I_{ij}^{obj} (1 - C_{ij})^\gamma f_{CE}(C_{ij}, \hat{C}_{ij}) \\ & + \sum_{i=0}^{S^2} \sum_{j=0}^B I_{ij}^{no-obj} (1 - C_{ij})^\gamma f_{CE}(C_{ij}, \hat{C}_{ij}) \end{aligned} \quad (4)$$

where I_{ij}^{obj} and I_{ij}^{no-obj} are mask factors that are the same as in L_{cls} , except I_{ij}^{no-obj} is 1 when there are no objects in the cell. f_{CE} is the cross entropy function defined in Equation 3 and $(1 - C_{ij})^\gamma$ is the focal loss term. We set the value $\gamma = 2$ as suggested in Lin et al. (2017).

L_{box} quantifies the coordinate difference between predicted and labeled bounding boxes. The most commonly used method for comparing the similarity between two bounding boxes is by computing the Intersection over Union (IoU), the ratio between the area of the intersection and the area of the union of two boxes. The more overlap, the greater the IoU , the more closely aligned are the two boxes. Then the loss based on IoU is just $L_{IoU} = 1 - IoU$. In YOLOv3, the IoU loss is weighted by a factor related to the area of the boxes to improve the performance for small boxes. Overall,

$$L_{box} = \sum_{i=0}^{S^2} \sum_{j=0}^B I_{ij}^{obj} (1 - IoU)(2 - \hat{w}_{ij}\hat{h}_{ij}) \quad (5)$$

where \hat{w}_{ij} and \hat{h}_{ij} are the width and height of the labeled box.

However, as we have described above, it is particularly tricky to label the LEs in an unambiguous way. Inside of a label box there are often multiple LEs and how to group the LEs is somewhat arbitrary. In the face of this ambiguity, the IoU loss is not able to properly reflect the properties of LEs and a traditional IoU may penalize good detections that split a LE-group differently than a visual inspector, but in just as valid a way. To enable the model to learn features inside the box and avoid penalizing fair choices that happen to be different than the ones implemented by the human labeler, we replace the IoU with the IoP , intersection over

Table 5. Hyperparameters of YOLOv3

Parameters	Value
Backbone	Darknet-53
Feature Strides	[8, 16, 32]
Anchor per scale	3
Initial learning rate	10^{-4}
Final learning rate	10^{-6}

prediction (where prediction is the area of the annotation label), in the evaluation phase. Simultaneously we generate larger annotation boxes for evaluation. In the training phase, we prepare annotations designed to separate each LE in a group. In evaluation, however, we use annotations designed to include all LEs in a LE-group, so that a different segmentation of the LE-group would not be penalized by our model.

4.2. Detection definition and Evaluation

While the loss minimization determines the parameter values of a model, some parameters have to be set by the user to select the optimal model for object detection. In the case of our CNN, in addition to the hyperparameter choices indicated in Table 5, this means choosing the thresholds for detection and classification above which a detection is considered valid. There are two thresholds that need to be chosen:

- the probabilistic classification score p_s threshold,
- the IoU threshold.

To evaluate the best threshold values we need to define what True/False Positives are based on the overlap of a label and a bounding box and the probabilistic classification of the object inside the box. We consider a detected bounding box as a true positive (TP) if

- the class predicted is the same as labeled (star or LE) and with score p_s larger than a threshold;
- the overlap between predicted and ground truth bounding boxes measured as their intersection over the union is larger than a threshold IoU .

Conversely, we count it as a false positive (FP), if

- class id is the same as labeled with p_s larger than a threshold, but IoU is less than the threshold.

Based on the properties of LEs discussed above, the standard IoU is not a good evaluation metric for LEs.

The LEs are extended features without clear boundaries, and valid prediction boxes that fall within an annotation box would have low IoU . Taking this into consideration, when searching for LEs, we replace the IoU with the IoP for LEs, while for the stars and “other” category we continue to use the standard IoU as the location and boundaries of the bounding box are generally not ambiguous. This reduces the number of False Negatives (FNs). Finally, predicted boxes that overlap with the same label box (see Figure 7) need to be consolidated so as to not to double count TPs.

Once we define the TP and FP, we are able to determine the receiver operating characteristic (ROC) curve, which indicates the number of TPs vs FPs at different thresholds. The two-dimensional area underneath the curve (AUC) measures the overall performance of the model: the larger the area, the better the model. In addition, we can also then calculate the precision-recall (PR) curve for various IoU (or IoP for LEs) and classification score thresholds.

Precision and recall are defined as

$$P = \frac{TP}{TP + FP} = \frac{TP}{N_{det}} \quad (6)$$

$$R = \frac{TP}{TP + FN} = \frac{TP}{N_{ann}} \quad (7)$$

where N_{det} is the total number of detected boxes, and N_{ann} is the total number of labeled boxes. Precision measures the fraction of positive detections that are correctly classified, while recall measures the completeness fraction. Precision and recall are often in tension: improving precision by increasing the classification and/or detection threshold, typically reduces recall, and vice versa. Therefore, the F1 score, defined as the harmonic mean of precision and recall $F_1 = 2 \frac{PR}{P+R}$, is often used as a measure of balance between precision and recall. The evaluation steps for our models are summarized in algorithm 1.

4.3. Training

We trained our model on the Google Colaboratory platform. We adopt a three-fold cross validation scheme in which 28 images containing LEs were randomly split into 10, 10 and 8 subsets. We kept one subset as a test set, and trained the model on the other two subsets. We shuffled the images once and repeated this process, thus obtaining six cross-validation sets. The results we present in section 5 represent the average of the results across these six cross-validation sets. We used an Adam optimizer (Kingma & Ba 2014) with an adaptive learning rate, setting the initial and final values to 10^{-4} and 10^{-6} respectively. We applied a learning rate schedule

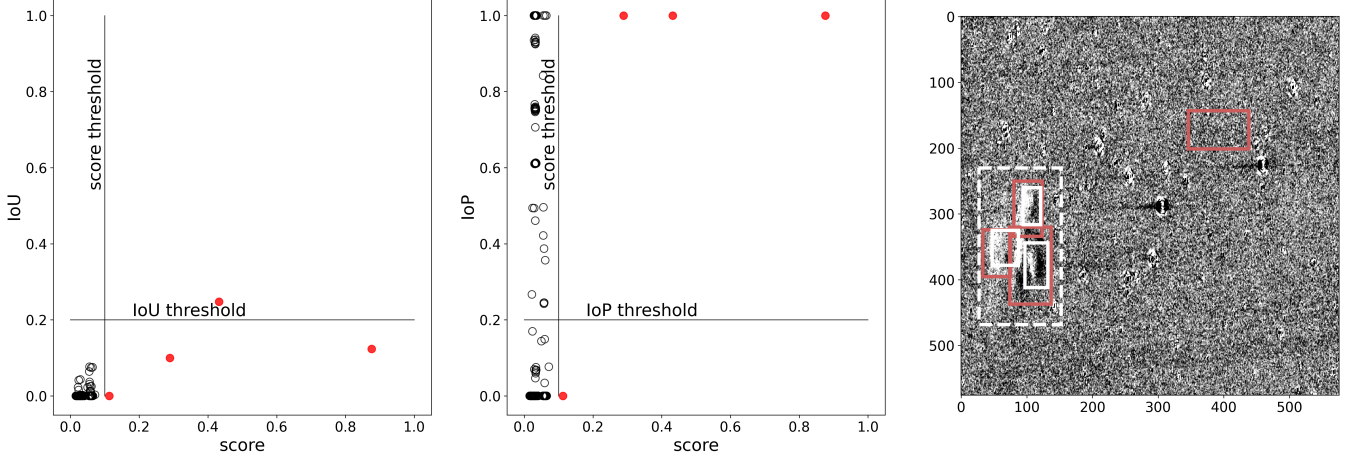


Figure 7. Predictions from YOLOv3 for an example image from our test set. The left panel shows a scatter plot of classification score vs. IoU —intersection over union—the traditional metric used in YOLO for training and evaluation, for all predicted bounding boxes. Four boxes pass the score threshold, set to 0.1; those are indicated by red circles in the left and center panels of this figure. However, the IoU value is $IoU < 0.2$, our chosen threshold, for three out of the four boxes. Based on the traditional IoU definition, three of these detections would be considered FPs. Due to the complexity of the LE morphology, the label boxes are somewhat arbitrary in their size and position and LEs could be split in different ways. In the right-most figure we mark the labels that we use in training phase (solid white boxes, typically smaller) and the labels that we use for model evaluation, that are designed to contain a light echo group in its entirety (white dashed box). While three of the four detection boxes do not pass the IoU threshold, two of them are in fact contained entirely inside of an evaluation label box. We calculate the IoP as the intersection of prediction and evaluation label over the area of the predicted box and replace the IoU with the IoP for model evaluation. In this example, the model successfully detected the LE group with three detections, all above the IoP threshold and this image contains only one FP, for which $IoP = 0$.

Algorithm 1: LE detection model evaluation

```

 $N_{ann} \leftarrow$  number of labeled objects ;
 $N_{det} \leftarrow$  number of predicted bounding boxes;
set classification score threshold ;
set  $IoP$  detection threshold;
 $N_{TP} \leftarrow 0$ ;
 $N_{FP} \leftarrow 0$ ;
for each predicted bounding box do
    if classification score  $>$  threshold then
        if  $IoP > IoP$  threshold then
            |  $N_{TP} \leftarrow N_{TP} + 1$ 
        end
        else
            |  $N_{FP} \leftarrow N_{FP} + 1$ 
        end
    end
end
 $P = N_{TP}/N_{det}$ ,
 $R = N_{TP}/N_{ann}$ ,
 $F1 = 2\frac{PR}{P+R}$ 

```

to improve the training progress as described in He et al. (2019). The learning rate is decreased from initial value following a cosine function.

5. RESULTS

Figure 8 shows our performance over multiple training epochs averaged over the six cross-validation sets.. The top panel in the figure shows the total loss (Equation 1) for the training and test sets. The training loss continues to decrease throughout all epochs, while the test loss reaches a minimum around 50 epochs and then rises slowly due to overfitting. The precision and recall for LEs on the test set are shown in the bottom panel. Precision and recall are calculated with a classification score threshold of 0.2 and IoP threshold of 0.1. After ~ 50 epochs, the $F1$ score stabilizes, and we choose the model state at 50 epochs as the final model for further evaluation.

Figure 7 shows an example of the YOLO predictions from our test set. Setting the score threshold to 0.1, there are four boxes above threshold. All but one of the four boxes have IoU values that are less than 0.1 and would be considered as FPs. But they are actually good detections: the model successfully detected several LEs belonging to the same LE-group within the labeled bounding box. Thus, the IoP replaces the IoU for LEs in the evaluation phase. Note that we use the IoP only for LEs. For the stars and “other” classes we use the IoU since the prediction box annotations are much less unambiguous, and the predictions are never in fact contained in the label boxes, so replacing the IoU is unnecessary.

The ROC and PR curves show the model performance for a given box-overlap threshold as the threshold on the classification probability is modified. The ROC and PR

curves for IoP (IoU) thresholds for LEs (stars) from 0 to 0.5 are shown in Figure 9. The top panel in Figure 9 shows that, for this particular cross-validation set, if we choose an $IoP > 0.1$, $R > 70\%$ recall is achieved at a precision of about $P \sim 95\%$ (score=0.4). This means that we have to tolerate a 5% FP rate to detect at least 70% of the LEs.

We note that both probability classification threshold and box-overlap threshold have to be set to very low values to achieve the desired performance (0.2 and 0.1 respectively for our best performing model). This implies that the classification score shall not be interpreted as a “probability” without performing a re-calibration; the classification score for stars and for LEs cannot be compared and thresholds should be set separately for each class.

With the large amount of astrophysical images to be produced with our target survey, LSST, we must control FPs in our model or else we will be overwhelmed with an unmanageable number of images to visually inspect. Or worse, we may deploy and waste follow up resources if we trust the automated detections without vetting them. As indicated in section 3, we prepared a training set that contains LEs in every image, but LEs are rare events and the vast majority of images from any surveys contain none. To test the robustness of the model, we added 100 images to the test set that contain stars, potentially artifacts, but no LEs. Following the same evaluation methods described in subsection 4.2, we found that precision drops with the score threshold. The rate of FPs grows sublinearly with the number of added images. The slope at score 0.5 is about 0.1, while at score 0.2, it is 0.3. We also found that these FPs largely appear near the edge of stars or where dipole structures, structures associated with poor image subtraction due to mismatched PSF between template and search image, or poor local alignment of the image, are present, see Figure 10.

Both our model and ALED (Bhullar et al. 2021), the only other automated LE detection method we are aware of, can achieve a high ($P \sim 90\%$) precision and high recall ($R \sim 90\%$) although, since the models were applied to different datasets, it is not straightforward to compare their performance at this time. We note that the final results reported for our model are on the median across the 6 cross-validation sets, while it appears that ALED did not perform cross validation. On a single set, our precision and recall can be as high as 0.9 simultaneously (see Figure 9), but perhaps the most fair comparison is that with the model reported in table 4 of Bhullar et al. (2021) as “ALED-m”: a precision $P = 1$, and a recall $R = 0.25$. When taking the median across all cross-

validation sets, at $P_{\text{median}} = 1$ we measure $R_{\text{median}} = 0.3$ for score and IoP thresholds of 0.7 and 0.2 respectively. While both datasets used for training the models are small, our dataset contains only $28\,576 \times 576$ images with LEs (before augmentation) compared to $175\,200 \times 200$ images in Bhullar et al. (2021). There are significant differences in the methodological approach. First, the ALED model identifies the presence of a light echo in an image (via binary classification) but does not locate the LE directly. The YOLO framework performs the detection and localization simultaneously, and returns class type as well as the exact coordinates of positions which is important if we envision further automation of the LE study pipeline, such as automatic selection of LEs for follow-up and automatic follow-up on robotic systems, an increasingly common practice in astrophysics (e.g., Street et al. 2018). We note, however, that the location of the LEs in the images can be estimated in a follow up step through the analysis of the ALED feature maps. In addition, the training of ALED requires a balanced dataset which must contain an equal number of LE and non-LE images, while our implementation can tolerate class imbalance through the application of a focal loss. Furthermore, the usage of region-based CNNs is particularly suited to application on image sequences, and applying our model to time-resolved LE image sequences is an on-going project.

All plots and associated model outputs can be found at the project GitHub repository AILE⁵.

6. CONCLUSION AND FUTURE WORK

In this paper, we described a novel LE detection model based on an AI object detection framework applied to a dataset of template-subtracted images from the ATLAS survey. As described in section 3, we labeled three classes: LEs (diffusive features from reflections of transients off of interstellar dust), stars (point-like sources), and “other” (a catch-all category used mostly for artifacts). We designed the detection model based on the architecture of YOLOv3, as described in section 4. Unlike traditional object detection tasks, LEs are diverse, extended features, their shapes vary over sky positions as well as time, their edges are not sharp and blend into the background, and their structure is complex. Thus, human labels can be quite subjective. Therefore, we modified the loss function used to train the model to incorporate both single LEs and LE-groups. We found that an $F1 \sim 0.7$ can be achieved at precision 70% even with an extremely limited training set, establishing

⁵ <https://github.com/xiaolng/AILE>

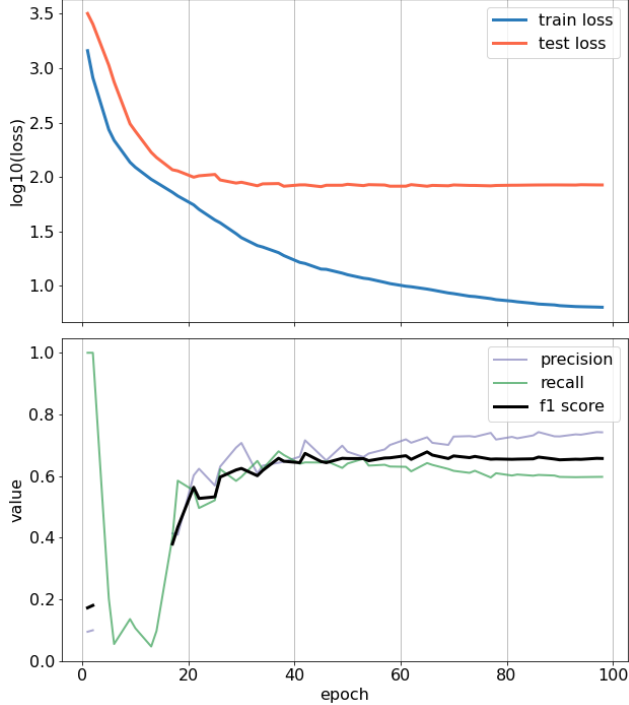


Figure 8. Training of YOLOv3, discussed in subsection 4.3. All curves in this figure represent averages across the 6 cross-validation datasets. The top panel shows the total loss for the training and test set, as labeled. The total loss is defined for YOLOv3 as the sum of classification and regression losses (see subsection 4.1). The test loss shows little improvement after about 50 epochs. The bottom plot shows the precision and recall for LEs as a function of training epoch, as well as the F_1 -score, as labeled. Precision and recall are calculated with a classification score threshold of 0.2 and IoP threshold of 0.2. The F_1 -score is the harmonic mean of precision and recall, demonstrating how a balance between the two is achieved near 50 epochs.

region-based CNNs as viable detection model architectures for localization and classification of LEs within an astronomical image.

This work demonstrates that modern region-based object detection architectures – i.e., architectures that identify and then classify regions of interest as opposed to sliding window, classification-only architectures that classify every sub-region of an image – produce detection accuracies for LEs that allow for the searching of extremely large upcoming data sets for these objects, a task which may very well be unfeasible with sliding-window classification models. And while it is true that these region-based models are rapidly evolving (YOLO itself is now at version 7, Wang et al. 2022, and other more recent models include Chen et al. 2019; Wu et al. 2019 for example), the core conceptual foundations are common to all such models. That is, the models pre-

sented in this paper have demonstrated that region-based models are applicable to astronomical data (low SNR, very high spatial resolution, etc.) for the detection of diffuse, morphologically complex features at the limit of the image SNR, suggesting that as these models are improved and new models (e.g., transformer-based architectures) are developed within the computer vision community, they will likely also be applicable to this problem when appropriate steps are taken to perform specific image preparation and definition of appropriate model architecture elements, including specialized loss functions.

While the aim of this paper was to provide a proof-of-concept, representing the first step toward the goal of building an AI-based LE detection platform in the Rubin LSST era, we have in fact made significant progress despite limitations in the presently available data. We achieved relatively high model accuracies ($F_1 \sim 0.7$) with a very limited training dataset size. We demonstrated that the number of false positives scales sublinearly with the number of images Figure 10 suggesting that our method can be successfully trained on and applied to large datasets without being overwhelmed by false positives or losing detection power. Furthermore, our model is also robust to significant class imbalance between labeled classes (~ 600 LEs, ~ 1300 stars).

Given that the ATLAS survey has relatively few LEs with uniquely characteristic image properties, this raises the question as to the transferability of the models presented in this work. We note however, that this is in fact a strength of our study since, while it is certainly true that any new data set will require new training and testing sets to be created and used to train the model, we have demonstrated that achieving reasonable testing accuracy is possible even with very few training examples with significant image noise and confounding non-LE artifacts and objects. We expect then that for upcoming data sets with higher SNR and more potential LE and non-LE objects on which to train, models can only be refined further. That is, since the models presented here are able to achieve reasonable accuracy, this provides confidence that at least comparable (but likely much higher) accuracy on larger and cleaner datasets will be possible.

For example, the ambitious scientific goals that LSST has set to pursue (Ivezic et al. 2019) impose unprecedented requirements on image quality, including PSF characterization, and control over systematics in the images (see for example The LSST Dark Energy Science Collaboration et al. 2018). Thus, the noise properties of the Rubin LSST images are expected to be far superior than current synoptic surveys, including ATLAS.

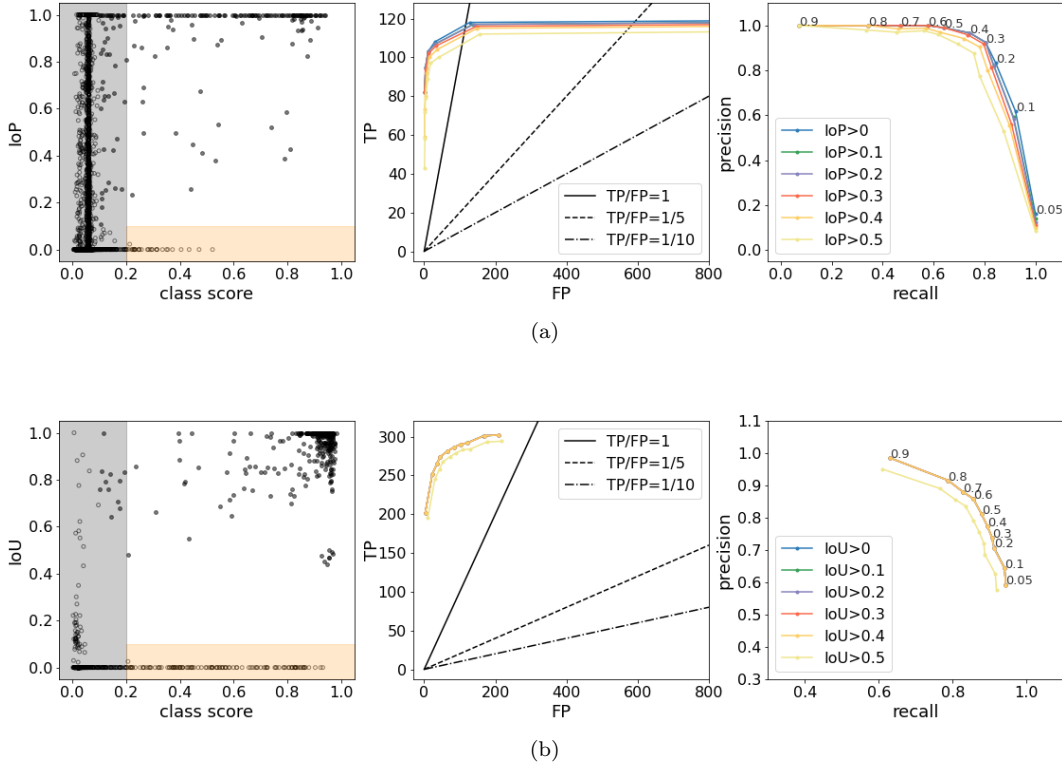


Figure 9. Test results from YOLOv3 for LEs (a) and stars (b) for a chosen cross-validation set. In both (a) and (b), the left panel shows a scatter plot of classification score vs. IoP (top, for LEs) or IoU (bottom, for stars) for all predicted bounding boxes. The middle panels show ROC curves and the right panels show PR curves. The grey regions in the left plots delimit the region of rejected predictions (below a score threshold of 0.1) and the orange regions represent the location where FPs are found (IoU or IoP smaller than 0.2). The ROC and PR are plotted for different thresholds of score (points along each curve) and different IoU or IoP (as labeled). In the ROC curve plots, the three black lines indicate a ratio of true positives to FPs of 1/1, 1/5 and 1/10. In the PR curve, gray lines join values obtained for the same score for different IoP thresholds. If we choose an $IoP > 0.1$ and a classification score threshold of 0.4, larger than 70% recall is achieved at a precision of about 95%. This means that we have to tolerate a 5% percent FPs to detect 70% of LEs. Because of the limited size of our test set, we leave studies of the influence of size, noise level and brightness of LEs on the precision/recall to future work.

By developing a model able to detect bright LEs in ATLAS images we have implicitly demonstrated that we will be able to push the detection limit to far fainter light echoes in the LSST era. Particularly, the 5-sigma limit of the survey is expected to be reached at a magnitude of $g \sim 24.5$ and $r \sim 24.0$,⁶ enabling the detection of far fainter LEs than the ATLAS survey; the plate scale of $0.2''$ will lead to seeing limited images at a site where sub-arcsecond seeing is common, enabling an accurate characterization of the shape of the PSF, leading to an LSST DIA pipeline expected to produce a minimum number of image artifacts, including in high density, high dust regions of the Galactic plane.⁷ Furthermore, the LSST survey will collect a median of 815 im-

ages for every position in the sky which will enable the creation of increasingly deeper templates over the lifetime of the survey, enabling progressive improvements in the detection of LEs in LSST.

In future work, we will expand our training/testing datasets with both additional observational data as well as additional augmentations and simulations to increase the accuracy of the model and its performance against a variety of morphologies and to push into ever lower SNR regimes.

Two important LE features remain to be explored: their color and their time evolution. The ATLAS data included five observing epochs, while each Rubin LSST field will be observed at least 800 times over the 10 years of the survey (with more epochs available in selected fields). The presence of a LE in multiple images collected at different times confirms the veracity of the LE and helps removing FPs in visual inspection (for exam-

⁶ <https://pstn-054.lsst.io>

⁷ <https://pstn-039.lsst.io/>

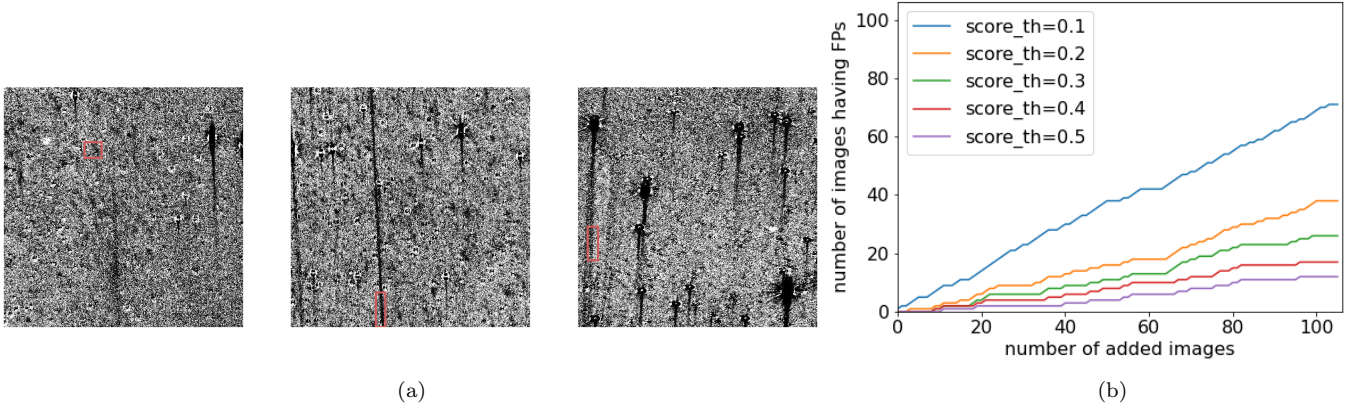


Figure 10. (a) Three types of common FPs from our implementation of YOLOv3 for LE searches in ATLAS images for the same cross-validation set used in Figure 9. FPs are primarily associated with two kinds of features in the images. “Dipole” structures, *i.e.* features in the difference image that show one bright and one dark side corresponding to moving objects, including LEs, but also, for example, asteroids generate FPs. This kind of FP is shown in the left most image in panel (a). The second kind of FPs are generated by saturated star streaks — middle and right images in panel (a). The class “other” is designed to train the model to recognize non LE artifacts, including these features. While this class suppresses the number of FPs compared to models trained on two classes only (LE and star), some of these artifacts are still incorrectly classified as LEs. Panel (b) shows that the rate of growth of FPs as a function of the number of images without LEs for which the model is asked to make prediction grows sublinearly for each of five score thresholds between 0.1 and 0.5. This figure is discussed in section 5.

ple those caused by light reflection inside of the telescope optical tube). Images taken from different epochs also provide an opportunity to study the time evolution of LEs. Leveraging the multi-epoch nature of the ATLAS dataset will be explored in future work. Furthermore, while ATLAS provides images in a single optical band, Rubin will observe in six filters. Exploiting the color properties of LEs in their detection and classification is also part of our plan for future work.

1 This paper was supported by the National Science Foundation
2 Grant No.2108841: Detecting and studying light
3 echoes in the era of Rubin and Artificial Intelligence
4 NSF; and No.1814993: An Astronomical Time Machine:
5 Light Echoes from Historic Supernovae. We acknowl-
6 edge the support of the Vera C. Rubin Legacy Survey
7 of Space Time Science Collaborations⁸ and particularly
8 of the Transient and Variable Star Science Collabora-
9 tion⁹ (TVS SC) that provided opportunities for collab-
10 oration and exchange of ideas and knowledge. This
11 work has made use of data from the Asteroid Terres-
12 trial impact Last Alert System (ATLAS) project. The
13 ATLAS project is primarily funded to search for near
14 earth asteroids through NASA grants NN12AR55G,
15 80NSSC18K0284, and 80NSSC18K1575; by products of
16 the Near-Earth Object (NEO) search include images and
17 catalogs from the survey area.

18 We used the following software packages: `astropy`
19 ([Astropy Collaboration et al. 2013, 2018](#)), `numpy` ([Harris](#)
20 [et al. 2020](#)), `pandas` ([Wes McKinney 2010](#); [pandas devel-](#)
21 [opment team 2020](#)), `matplotlib` ([Hunter 2007](#)), `opencv`
22 ([Bradski 2000](#)), `TensorFlow` ([Abadi et al. 2015](#)), and
23 `labelme` ([Wada 2016](#)).

24 Our dataset is augmented using modules in GitHub
25 repository ¹⁰. The implementation of YOLOv3 arche-
26 tecture is based on the GitHub repository ¹¹

REFERENCES

- Abadi, M., Agarwal, A., Barham, P., et al. 2015, TensorFlow: Large-Scale Machine Learning on Heterogeneous Systems. <https://www.tensorflow.org/>
- Alard, C., & Lupton, R. H. 1998, ApJ, 503, 325, doi: [10.1086/305984](https://doi.org/10.1086/305984)
- Andrews, J., Sugerman, B., Clayton, G. C., et al. 2011, The Astrophysical Journal, 731, 47
- Astropy Collaboration, Robitaille, T. P., Tollerud, E. J., et al. 2013, A&A, 558, A33, doi: [10.1051/0004-6361/201322068](https://doi.org/10.1051/0004-6361/201322068)
- Astropy Collaboration, Price-Whelan, A. M., Sipőcz, B. M., et al. 2018, AJ, 156, 123, doi: [10.3847/1538-3881/aabc4f](https://doi.org/10.3847/1538-3881/aabc4f)
- Bhullar, A., Ali, R., & Welch, D. 2021, Astronomy & Astrophysics
- Bode, M., & Evans, A. 1985, Astronomy and Astrophysics, 151, 452
- Bond, H. E., Henden, A., Levay, Z. G., et al. 2003, Nature, 422, 405
- Bradski, G. 2000, Dr. Dobb's Journal of Software Tools
- Cappellaro, E., Patat, F., Mazzali, P., et al. 2001, The Astrophysical Journal Letters, 549, L215
- Chan, M. C., & Stott, J. P. 2019, Monthly Notices of the Royal Astronomical Society, 490, 5770
- Chen, K., Wang, J., Pang, J., et al. 2019, arXiv preprint arXiv:1906.07155
- Couderc, P. 1939, in Annales d'Astrophysique, Vol. 2, 271
- Crotts, A. P. 1988, The Astrophysical Journal, 333, L51
- . 2015, The Astrophysical Journal Letters, 804, L37
- Crotts, A. P., & Yourdon, D. 2008, The Astrophysical Journal, 689, 1186
- Crotts, A. P. S. 1992, ApJL, 399, L43, doi: [10.1086/186602](https://doi.org/10.1086/186602)
- Davies, A., Serjeant, S., & Bromley, J. M. 2019, Monthly Notices of the Royal Astronomical Society, 487, 5263
- Drozdov, D., Leising, M., Milne, P., et al. 2015, The Astrophysical Journal, 805, 71
- Everingham, M., Van Gool, L., Williams, C. K., Winn, J., & Zisserman, A. 2010, International journal of computer vision, 88, 303
- Finn, K., Bianco, F. B., Modjaz, M., Liu, Y.-Q., & Rest, A. 2016, The Astrophysical Journal, 830, 73
- Gallagher, J. S., Sugerman, B., Clayton, G. C., et al. 2012, The Astrophysical Journal, 753, 109
- Girshick, R. 2015, in Proceedings of the IEEE international conference on computer vision, 1440–1448
- Girshick, R., Donahue, J., Darrell, T., & Malik, J. 2014, in Proceedings of the IEEE conference on computer vision and pattern recognition, 580–587
- Harris, C. R., Millman, K. J., van der Walt, S. J., et al. 2020, Nature, 585, 357, doi: [10.1038/s41586-020-2649-2](https://doi.org/10.1038/s41586-020-2649-2)
- Havlen, R. 1972, Astronomy and Astrophysics, 16, 252
- He, K., Zhang, X., Ren, S., & Sun, J. 2016, in Proceedings of the IEEE conference on computer vision and pattern recognition, 770–778
- He, T., Zhang, Z., Zhang, H., et al. 2019, in Proceedings of the IEEE/CVF Conference on Computer Vision and Pattern Recognition, 558–567
- Hunter, J. D. 2007, Computing in Science & Engineering, 9, 90, doi: [10.1109/MCSE.2007.55](https://doi.org/10.1109/MCSE.2007.55)
- Ivezić, Ž., Kahn, S. M., Tyson, J. A., et al. 2019, The Astrophysical Journal, 873, 111
- Kastner, J. H., Weintraub, D. A., Merrill, K., & Gatley, I. 1998, The Astronomical Journal, 116, 1412
- Kastner, J. H., Weintraub, D. A., Zuckerman, B., et al. 1992, The Astrophysical Journal, 398, 552
- Kingma, D. P., & Ba, J. 2014, arXiv preprint arXiv:1412.6980
- Krause, O., Birkmann, S. M., Usuda, T., et al. 2008a, Science, 320, 1195
- Krause, O., Tanaka, M., Usuda, T., et al. 2008b, Nature, 456, 617
- LeCun, Y., Bengio, Y., & Hinton, G. 2015, nature, 521, 436
- LeCun, Y., Boser, B., Denker, J. S., et al. 1989, Neural computation, 1, 541
- Lin, T.-Y., Goyal, P., Girshick, R., He, K., & Dollár, P. 2017, in Proceedings of the IEEE international conference on computer vision, 2980–2988
- Lin, T.-Y., Maire, M., Belongie, S., et al. 2014, in European conference on computer vision, Springer, 740–755
- Liu, J.-F., Bregman, J. N., & Seitzer, P. 2003, The Astrophysical Journal, 582, 919
- Liu, W., Zhu, M., Dai, C., et al. 2019, Research in Astronomy and Astrophysics, 19, 042
- Maund, J. R., & Smartt, S. J. 2005, Monthly Notices of the Royal Astronomical Society, 360, 288
- Miller, A., Smith, N., Li, W., et al. 2010, The Astronomical Journal, 139, 2218
- Neubeck, A., & Van Gool, L. 2006, in 18th International Conference on Pattern Recognition (ICPR'06), Vol. 3, IEEE, 850–855
- Norgaard-Nielsen, H. U., Hansen, L., Jorgensen, H. E., Aragon Salamanca, A., & Ellis, R. S. 1989, Nature, 339, 523, doi: [10.1038/339523a0](https://doi.org/10.1038/339523a0)
- Oksuz, K., Cam, B. C., Kalkan, S., & Akbas, E. 2020, IEEE transactions on pattern analysis and machine intelligence
- Ortiz, J., Sugerman, B., de La Cueva, I., et al. 2010, Astronomy & Astrophysics, 519, A7
- Otsuka, M., Meixner, M., Panagia, N., et al. 2011, The Astrophysical Journal, 744, 26

- pandas development team, T. 2020, pandas-dev/pandas: Pandas, latest, Zenodo, doi: [10.5281/zenodo.3509134](https://doi.org/10.5281/zenodo.3509134)
- Patat, F. 2005, Monthly Notices of the Royal Astronomical Society, 357, 1161
- Patat, F., Benetti, S., Cappellaro, E., & Turatto, M. 2006, Monthly Notices of the Royal Astronomical Society, 369, 1949
- Phillips, A. C., & Davis, L. E. 1995, in Astronomical Society of the Pacific Conference Series, Vol. 77, Astronomical Data Analysis Software and Systems IV, ed. R. A. Shaw, H. E. Payne, & J. J. E. Hayes, 297
- Prieto, J., Rest, A., Bianco, F., et al. 2014, The Astrophysical Journal Letters, 787, L8
- Quinn, J. L., Garnavich, P. M., Li, W., et al. 2006, The Astrophysical Journal, 652, 512
- Redmon, J., Divvala, S., Girshick, R., & Farhadi, A. 2016, in Proceedings of the IEEE conference on computer vision and pattern recognition, 779–788
- Redmon, J., & Farhadi, A. 2018, arXiv preprint arXiv:1804.02767
- Ren, S., He, K., Girshick, R., & Sun, J. 2015, in Advances in neural information processing systems, 91–99
- Rest, A., Sinnott, B., Welch, D. L., et al. 2011, ApJ, 732, 2, doi: [10.1088/0004-637X/732/1/2](https://doi.org/10.1088/0004-637X/732/1/2)
- Rest, A., Suntzeff, N. B., Olsen, K., et al. 2005, Nature, 438, 1132
- Rest, A., Becker, A., Bergmann, M., et al. 2007, in American Astronomical Society Meeting Abstracts, Vol. 211, 107–02
- Rest, A., Welch, D., Suntzeff, N., et al. 2008a, The Astrophysical Journal Letters, 681, L81
- Rest, A., Matheson, T., Blondin, S., et al. 2008b, The Astrophysical Journal, 680, 1137
- Rest, A., Foley, R., Sinnott, B., et al. 2011, The Astrophysical Journal, 732, 3
- Rest, A., Prieto, J., Walborn, N., et al. 2012, Nature, 482, 375
- Ritchey, G. 1901, The Astrophysical Journal, 14 —. 1902, The Astrophysical Journal, 15
- Russakovskiy, O., Deng, J., Su, H., et al. 2015, International journal of computer vision, 115, 211
- Sabour, S., Frosst, N., & Hinton, G. E. 2017, Advances in neural information processing systems, 30
- Sánchez Fernández, I., Yang, E., Calvachi, P., et al. 2020, PloS one, 15, e0232376
- Schmidt, B. P., Kirshner, R. P., Leibundgut, B., et al. 1994, ApJL, 434, L19, doi: [10.1086/187562](https://doi.org/10.1086/187562)
- Smith, N., Rest, A., Andrews, J. E., et al. 2018a, Monthly Notices of the Royal Astronomical Society, 480, 1457
- Smith, N., Andrews, J. E., Rest, A., et al. 2018b, Monthly Notices of the Royal Astronomical Society, 480, 1466
- Sparks, W., Macchetto, F., Panagia, N., et al. 1999, The Astrophysical Journal, 523, 585
- Street, R. A., Bowman, M., Saunders, E. S., & Boroson, T. 2018, in Society of Photo-Optical Instrumentation Engineers (SPIE) Conference Series, Vol. 10707, Software and Cyberinfrastructure for Astronomy V, ed. J. C. Guzman & J. Ibsen, 1070711, doi: [10.1117/12.2312293](https://doi.org/10.1117/12.2312293)
- Sugerman, B., & Lawrence, S. 2016, The Astronomer's Telegram, 8890, 1
- Sugerman, B. E. 2003, The Astronomical Journal, 126, 1939 —. 2005, The Astrophysical Journal Letters, 632, L17
- Sugerman, B. E., & Crots, A. P. 2002, The Astrophysical Journal Letters, 581, L97
- Sugerman, B. E., Andrews, J. E., Barlow, M. J., et al. 2012, The Astrophysical Journal, 749, 170
- Sultana, F., Sufian, A., & Dutta, P. 2020, Intelligent Computing: Image Processing Based Applications, 1
- Suntzeff, N., Heathcote, S., Weller, W., et al. 1988, Nature, 334, 135
- Swope, H. H. 1940, Harvard College Observatory Bulletin, 913, 11
- The LSST Dark Energy Science Collaboration, Mandelbaum, R., Eifler, T., et al. 2018, The LSST Dark Energy Science Collaboration (DESC) Science Requirements Document, arXiv, doi: [10.48550/ARXIV.1809.01669](https://arxiv.org/abs/1809.01669)
- Tonry, J., Denneau, L., Heinze, A., et al. 2018, Publications of the Astronomical Society of the Pacific, 130, 064505
- Tylenda, R. 2004, Astronomy & Astrophysics, 414, 223
- Van Dyk, S. D. 2013, The Astronomical Journal, 146, 24
- Van Dyk, S. D., Li, W., & Filippenko, A. V. 2006, Publications of the Astronomical Society of the Pacific, 118, 351
- Van Dyk, S. D., Lee, J. C., Anderson, J., et al. 2015, The Astrophysical Journal, 806, 195
- Vaswani, A., Shazeer, N., Parmar, N., et al. 2017, in Advances in neural information processing systems, 5998–6008
- Wada, K. 2016, labelme: Image Polygonal Annotation with Python, <https://github.com/wkentaro/labelme>
- Wang, C.-Y., Bochkovskiy, A., & Liao, H.-Y. M. 2022, arXiv preprint arXiv:2207.02696
- Wang, X., Li, W., Filippenko, A. V., et al. 2008, The Astrophysical Journal, 677, 1060
- Welch, D., Clayton, G. C., Campbell, A., et al. 2007, The Astrophysical Journal, 669, 525
- Wells, D. C., & Greisen, E. W. 1979, in Image Processing in Astronomy, 445

Wes McKinney. 2010, in Proceedings of the 9th Python in
Science Conference, ed. Stéfan van der Walt & Jarrod
Millman, 56 – 61, doi: [10.25080/Majora-92bf1922-00a](https://doi.org/10.25080/Majora-92bf1922-00a)

Wu, Y., Kirillov, A., Massa, F., Lo, W.-Y., & Girshick, R.
2019, Detectron2,
<https://github.com/facebookresearch/detectron2>
Yang, Y., Wang, L., Baade, D., et al. 2017, The
Astrophysical Journal, 834, 60
Zhao, Z.-Q., Zheng, P., Xu, S.-t., & Wu, X. 2019, IEEE
transactions on neural networks and learning systems, 30,
3212